Research Square

Preprints are preliminary reports that have not undergone peer review.
They should not be considered conclusive, used to inform clinical practice,
or referenced by the media as validated information.

Beyond the Surface: Inferring Internal Battery Pressure and Temperature Using Optical Fibre Sensing and Machine Learning

Micael Nascimento

micaelnascimento@ua.pt

University of Aveiro https://orcid.org/0000-0001-9746-9152

Lucca Matuck

University of Aveiro https://orcid.org/0000-0001-9792-4768

João Pires

University of Aveiro

José Mendes

University of Aveiro

Marta Ferreira

University of Aveiro

Article

Keywords: Lithium-ion Batteries, Sodium-ion Batteries, Physical Optical Fibre Sensors, Virtual Sensors, Deep Temporal Models

Posted Date: March 3rd, 2026

DOI: https://doi.org/10.21203/rs.3.rs-8651829/v1

License: This work is licensed under a Creative Commons Attribution 4.0 International License.
Read Full License

Additional Declarations: There is **NO** Competing Interest.

Beyond the Surface: Inferring Internal Battery Pressure and Temperature Using Optical Fibre Sensing and Machine Learning

Lucca Matuck[1], João P. Pires[1], José F. F. Mendes[1], Marta S. Ferreira[1], Micael Nascimento[1]*

[1]i3N and Department of Physics, University of Aveiro, Campus de Santiago, 3810-193 Aveiro, Portugal

*Corresponding authors: micaelnascimento@ua.pt

Abstract

Virtual sensing of internal battery parameters is essential for improving safety and control without invasive instrumentation. We combine embedded optical fibre sensors with deep temporal models to reconstruct internal temperature and pressure evolution of lithium-ion (LIB) and sodium-ion (SIB) batteries. The physical sensors data provide ground truth targets, while surface and ambient temperature, voltage, current, and charge are used as features. Bayesian optimisation identifies chemistry-dependent temporal convolutional network configurations, with LIB favouring shorter input windows and larger convolutional kernels, while SIB benefits from longer windows and smaller kernels. The resulting virtual sensors achieve high-fidelity reconstruction across both chemistries. Internal temperature and pressure reached RMSE of 0.075 °C and 0.288 °C, and 0.048 bar and 0.013 bar, for the LIB and SIB, respectively. Residual, cycle-level, and cycle-resolved analyses demonstrate stable generalisation, and permutation-importance profiles confirm reliance on physically meaningful electro-thermal features, enabling non-invasive, chemistry-adapted monitoring for battery management systems.

Keywords: Lithium-ion Batteries; Sodium-ion Batteries; Physical Optical Fibre Sensors; Virtual Sensors; Deep Temporal Models

Main

The rapid proliferation of rechargeable batteries has become a keystone of the ongoing energy transition, with several applications from electric vehicles to stationary storage systems [1–3]. Among the available chemistries, lithium-ion batteries (LIBs) currently dominate the market due to their high energy density and well-established manufacturing ecosystem [4–6]. However, concerns regarding cost, resource scarcity, and safety have motivated the exploration of alternative chemistries such as sodium-ion batteries (SIB), which offer lower material costs and improved sustainability [7–10]. Despite their differences in electrochemical composition, both chemistries share a fundamental challenge: the difficulty of directly accessing and monitoring internal physical state parameters that play a critical role in their performance, degradation, and safety levels during operation, such as temperature, pressure, and mechanical stress [11–16].

Conventional battery management systems (BMS) rely almost exclusively on external electrical signals (voltage, current, and surface temperature) to infer internal conditions through empirical models or state observers [17,18]. Although conventional approaches perform adequately under standard operation, they provide only a partial view of the cell's internal conditions, capturing external electrical behaviour but missing the underlying thermo-mechanical interactions that govern its dynamic response over cycling [17,19,20]. Even during nominal cycling, internal pressure and temperature exhibit informative data that cannot be reliably inferred from terminal electrical signals alone [21–26], motivating non-invasive sensing and data-driven reconstruction from standard external measurements.

Optical fibre sensors (OFS) have proven to be an exceptional tool for in-situ battery monitoring due to their sub-millimetre scale, immunity to electromagnetic interference, multiparameter monitoring capabilities, and ability to withstand harsh electrochemical environments [27,28]. Embedded fibre Bragg gratings (FBGs) and Fabry–Perot interferometers (FPIs) can simultaneously and precisely track strain, pressure, and temperature, enabling access to internal physical parameters under operation [28–35]. However, the integration of such sensors is typically limited to laboratory environments, as their embedding is still a challenge for real-world applications. To overcome this limitation, it becomes crucial to translate the internal information provided by them into a non-invasive framework, enabling the design of virtual sensors that can infer the internal conditions of the battery without requiring physical instrumentation inside the cell. This goal can be achieved through the development of data-driven models capable of predicting internal states solely from external and easily measurable quantities.

Recent advances in machine learning (ML) have enabled data-driven inference of key battery states from standard non-invasive measurements [36–39]. ML has been widely applied to estimate the state of charge (SoC) [40–46], state of health (SoH) [46–50], and

temperature-related states [51–55], typically using electrical and surface thermal signals as inputs. Particularly, in the temperature-estimation studies, supervision relies on non-invasive temperature measurements (surface-mounted sensors), rather than experimentally measured in-cell internal temperature ground truth. When "internal/core temperature" is considered, it is typically introduced as a model/observer-inferred state (e.g., electro-thermal models and filtering/observers) rather than being learned directly from invasive internal-temperature targets. Moreover, internal pressure has remained largely absent from ML-based virtual sensing studies, despite its strong relevance to safety and degradation. These gaps motivate ML frameworks that incorporate reliable experimental targets for internal thermo-mechanical states.

In this work, we present a cross-chemistry ML framework that integrates a hybrid optical fibre sensing configuration (FPI + FBG) with deep temporal models to predict the internal temperature (T_{in}) and hydrostatic pressure variation (ΔP_{in}) of both LIBs and SIBs. The physical sensors provide ground-truth calibration data for model training, while the predictive models rely exclusively on external features, ensuring applicability to real-world BMS environments. The methodology leverages Bayesian optimization (Optuna) to automatically tune the network architecture and learning parameters for each chemistry, highlighting how the temporal dynamics and nonlinearities differ between both LIBs and SIBs.

To the best of our knowledge, this study provides the first ML demonstration of simultaneous ΔP_{in} and T_{in} estimation grounded in embedded hybrid optical sensing, and the first cross-chemistry virtual-sensing analysis directly comparing LIBs and SIBs under identical modelling conditions. By placing the two chemistries within the same acquisition and learning framework, we reveal how their thermo-mechanical responses and optimal temporal architectures diverge, while still achieving high-fidelity virtual sensing from non-invasive signals alone. Besides enabling this comparison, the proposed framework establishes a transferable foundation for data-driven diagnostics and digital twins of electrochemical cells, in which invasive optical measurements are used during development to train virtual sensors that subsequently operate using only standard BMS instrumentation. In doing so, it contributes to the development of safer, more transparent, and more adaptive BMS, allowing internal behaviour to be learned without requiring permanent internal physical sensors.

Results

To evaluate the proposed virtual-sensing framework across different battery chemistries, we quantified how effectively external electrical and thermal signals can reconstruct the T_{in} and ΔP_{in} measured by the instrumented FPI+FBG sensors. **Fig. 1** summarises the workflow from instrumented batteries and data acquisition to Temporal Convolutional Network (TCN) training and fully virtual sensing based only on non-invasive features. LIB and SIB datasets were acquired and analysed under identical modelling conditions, enabling a direct comparison of temporal dynamics, correlation structures, predictive accuracy, and error patterns. The following subsections present the optimised temporal architectures, the statistical properties of the input variables, and the resulting prediction performance, highlighting the chemistry-dependent mechanisms that govern internal state reconstruction.

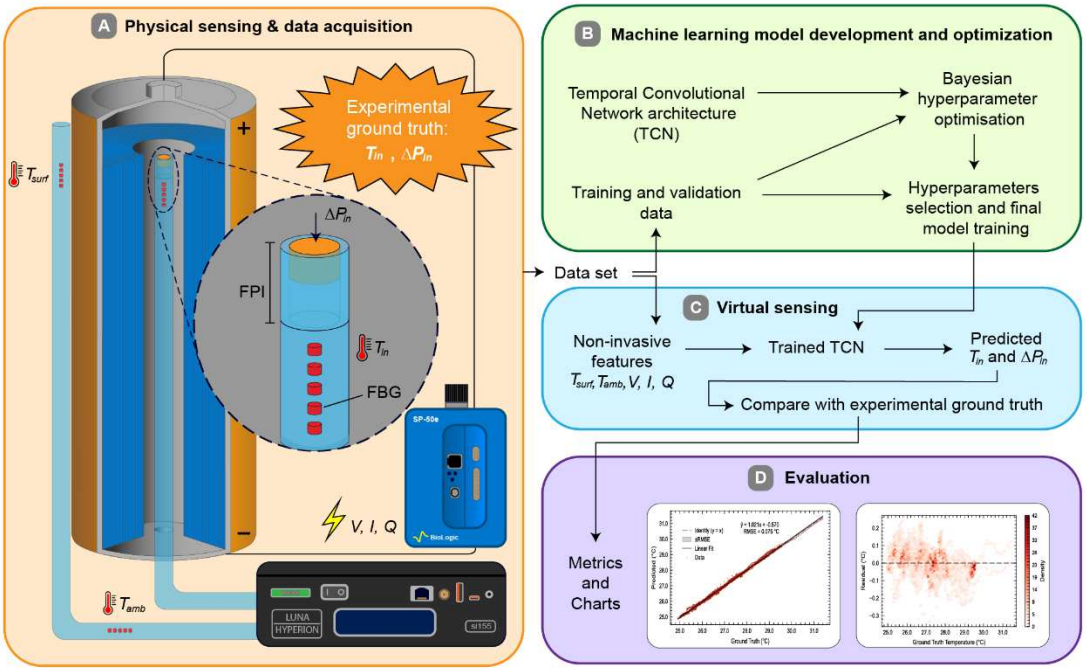


Fig. 1 Overview of optical-ground-truth–trained virtual sensing of internal battery states. (A) Physical sensing and data acquisition: a hybrid embedded OFS (FBG–FPI) provides experimentally measured internal ground truth, namely internal temperature T_{in} and pressure variation ΔP, while non-invasive signals are recorded simultaneously (surface temperature T_{surf}, ambient temperature T_{amb}, voltage V, current I, and cumulative charge Q). (B) Model development and optimisation: a Temporal Convolutional Network (TCN) is tuned via Bayesian hyperparameter optimisation and trained/validated on cycle-resolved time-series datasets. (C) Virtual sensing: the trained TCN reconstructs T_{in} and ΔP from the non-invasive inputs and its predictions are compared against the experimental ground truth. (D) Evaluation: performance is quantified using standard regression metrics and diagnostic plots (e.g., parity and residual analyses), supporting non-invasive, chemistry-adapted monitoring of internal battery states.

Chemistry-dependent optimisation of temporal models

Bayesian optimisation resulted in two distinct temporal convolutional configurations for the LIB and SIB datasets, revealing clear differences in how each chemistry encodes its internal thermo-mechanical dynamics. For the LIB, the optimal model emphasises high representational capacity over short time scales, while still maintaining a moderate temporal receptive field. In contrast, the SIB optimum converges to a more compact convolutional block operating on a longer input context, indicating a stronger reliance on longer-term temporal integration. The complete set of tuned hyperparameters is provided in the *Supplementary Information* (SI) file, in **Table S1**.

Training and validation curves for both models show stable convergence, with validation loss decreasing sharply in the first epochs and then fluctuating around a plateau while training loss continues to decrease, and can be observed in **Fig. S1**. This behaviour indicates a persistent train–validation gap, but no late-epoch divergence or instability. Furthermore, these results indicate that LIB behaviour is best captured by a wider, higher-capacity temporal block acting on a shorter window, whereas SIB behaviour benefits from a narrower block applied over a longer window. This divergence in optimal architectures anticipates the chemistry-specific correlation patterns seen in **Fig. 2** and the performance differences highlighted by the parity and error-structure analysed in **Figs. 3–5**.

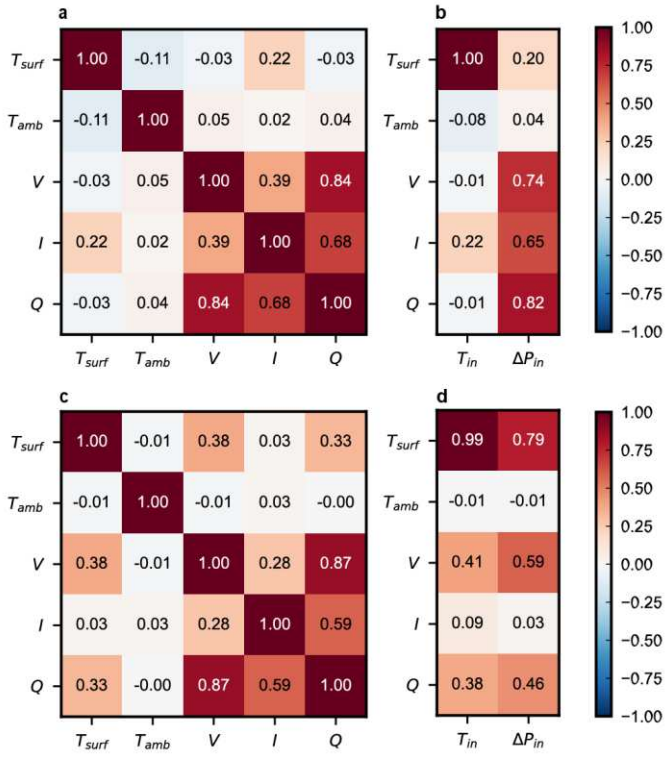


Fig. 2 Pearson-correlation structure of external measurements and internal states for LIB and SIB. **a.** Feature–feature correlation matrix for the LIB dataset, including surface temperature T_{surf}, ambient temperature T_{amb}, voltage V, current I, and cumulative charge Q. Electrical variables form a strongly coupled block, whereas surface temperature shows only weak correlations with the electrical features. **b.** Feature–target correlations for LIB, relating external measurements to internal temperature T_{in} and pressure variation ΔP_{in}; T_{in} is almost perfectly correlated with T_{surf}, while ΔP_{in} depends primarily on electrical variables. **c.** Corresponding feature–feature matrix for the SIB dataset, showing a similar electrical block and weak-to-moderate correlations between T_{surf} and electrical variables. **d.** Feature–target correlations for SIB, where T_{in} remains tightly linked to T_{surf} but also exhibits moderate associations with voltage and charge; ΔP_{in} displays moderate-to-strong correlation with T_{surf} and only moderate correlations with electrical variables. Numbers in each cell indicate the Pearson coefficient, and colour bars encode correlation strength.

Input feature structure and cross-chemistry correlations

The statistical structure of the external measurements reveals how each chemistry encodes internal thermo-mechanical states into surface-accessible signals. **Fig. 2** summarises the Pearson correlations between external features and between each feature and the two internal targets for both batteries. The feature–feature matrix of the LIB shown in **Fig. 2a** exposes that the electrical variables are strongly and coherently coupled. Voltage (V), current (I), and cumulative charge (Q) form a tightly coupled group ($|r| \geq 0.4$-0.8), indicating that they co-evolve along charge–discharge cycles. Surface temperature (T_{surf}) shows only weak coupling to the electrical variables: it displays a small positive correlation with I ($r \approx 0.22$) and is essentially uncorrelated with V and Q ($r \approx -0.03$ for both). This indicates that the surface thermal response is only loosely tied to the instantaneous

electrical conditions and provides information that is largely complementary to the electrical block.

The feature–target matrix presented in **Fig. 2b** reveals a very sharp encoding of T_{in}, which is almost perfectly correlated with T_{surf} ($r \approx 1.00$) and essentially uncorrelated with the remaining variables. This indicates that instantaneous T_{in} can be inferred with high fidelity from a single external thermal channel. Accordingly, T_{in} serves as a useful sanity-check target, whereas ΔP_{in} reconstruction provides a more stringent test of electro-thermo-mechanical encoding from non-invasive signals. In contrast, ΔP_{in} depends on a broader combination of electrical and electro-thermal indicators: it shows strong positive correlations with Q ($r \approx 0.82$), V ($r \approx 0.74$), and I ($r \approx 0.65$), while the thermal channels are only weakly informative. The ΔP_{in} in the LIB is therefore encoded primarily through electrochemical load and charge-storage history rather than purely thermal effects.

Regarding the SIB, the feature–feature correlations (**Fig. 2c**) display a similar electrical cluster, with pronounced coupling between V, I, and Q (e.g., $r \approx 0.87$ between V and Q). The T_{surf} value shows weak-to-moderate correlations with the electrical variables: it is essentially uncorrelated with I ($r \approx 0.03$) but exhibits slightly higher correlations with V and Q ($r \approx 0.38$ and $r \approx 0.33$, respectively) than the tests with the LIB chemistry. Overall, the thermal channels therefore provide information that is largely complementary rather than redundant with respect to the electrical features.

From **Fig. 2d**, the features–target correlations highlight a distinct regime. T_{in} values remain strongly correlated with T_{surf} ($r \approx 0.99$), but, unlike in LIB, it also exhibits moderate associations with V and Q ($r \approx 0.38$–0.41). This indicates that the T_{in} of Na-ion chemistry reflects not only the instantaneous surface thermal state but also the electrical history of the battery. Furthermore, the ΔP_{in} shows only moderate correlations with V and Q ($r \approx 0.4$–0.5) and negligible correlation with I, pointing to a smoother and less sharply driven mechanical response. Notably, pressure values exhibit a more pronounced correlation with T_{surf} than in LIB, indicating a stronger thermo-mechanical contribution to SIB pressure dynamics.

Taken together, these correlation structures indicate two complementary encoding strategies. Internal states of LIB chemistry are tightly tied to highly redundant instantaneous measurements, allowing the model to exploit strong short-range signs. On the other hand, internal states of SIB are instead distributed over weaker but more heterogeneous relationships, particularly between T_{in} and electrical variables, and between pressure and the thermal channel, motivating the longer temporal window and distinct architecture selected for this chemistry.

Predictive performance across chemistries

The optimised models achieve high-fidelity reconstruction of T_{in} and ΔP_{in} for both chemistries, suggesting that the learned representations capture the dominant temporal dependencies. **Fig. 3** presents parity plots between predicted and ground-truth values. A comprehensive set of error metrics, including Mean Absolute Error (MAE), Root Mean Square Error (RMSE), R^2, and normalised Root Mean Square Error (NRMSE), computed under two normalisations: by the test-set standard deviation ($NRMSE_{std}$) and by the test-set peak-to-peak range ($NRMSE_{range}$), are reported in the SI file (**Table S2**). Together, these complementary metrics assess both accuracy and generalization performance across different operating regimes.

The model revealed extremely accurate internal temperature predictions for the LIB, as shown in **Fig. 3 a**. The parity plot closely follows the identity line, with RMSE ≈ 0.08 °C and $NRMSE_{std} \approx 0.06$. The coefficient of determination is $R^2 \approx 0.996$, and the residual distribution is sharply peaked with very small tails (SI, **Fig. S2**), indicating that large deviations are sporadic. Internal pressure predictions (**Fig. 3b**) still achieve strong performance, with RMSE ≈ 0.05 bar, $R^2 \approx 0.97$, and $NRMSE_{std} \approx 0.17$, but exhibit a broader dispersion band than temperature, reflecting increased nonlinearity and a more complex temporal encoding of pressure-related dynamics.

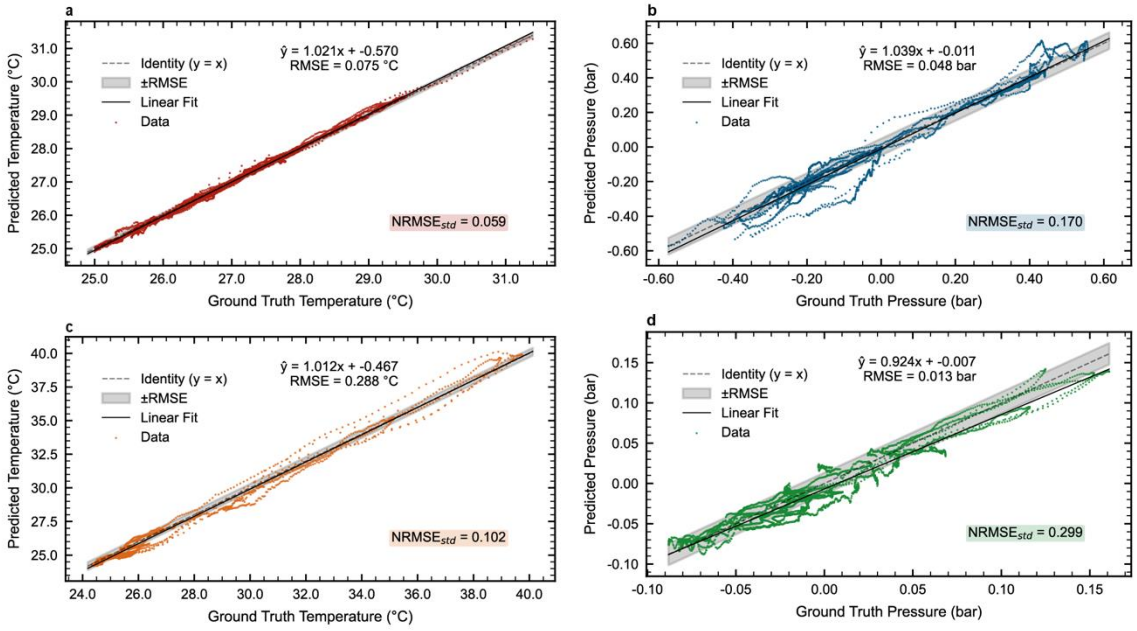


Fig. 3 a. Parity plots comparing predicted and measured internal temperature and pressure for LIB and SIB chemistries. **a.** LIB internal temperature predictions versus ground truth, with the identity line (dashed), linear regression fit (solid), ±RMSE band (shaded), and individual data points. The cloud closely follows the

identity, indicating very small dispersion. **b.** LIB internal pressure, showing a wider but still well-aligned cloud, with increased spread during strongly dynamic segments. **c.** SIB internal temperature, with larger deviations from the identity line and increased scatter relative to LIB temperature. **d.** SIB internal pressure, characterised by small absolute errors over a narrow pressure range and a clear, though slightly weaker, linear trend than LIB pressure. Insets report the linear fit and RMSE for each task, and the normalised RMSE with respect to the test-set standard deviation ($NRMSE_{std}$) is highlighted in each panel. Exact numerical metrics are summarised in the SI file (Table S2).

Concerning the SIB, internal temperature (**Fig. 3c**) presents larger deviations, with RMSE ≈ 0.29 °C and $NRMSE_{std}$ ≈ 0.10, while still preserving a high R^2 (≈ 0.99). In absolute terms, this corresponds to an RMSE roughly 3.8 times larger than for LIB temperature estimation. The error structure shows a complementary behaviour where ΔP_{in} is predicted with small absolute errors (**Fig. 3d**), with RMSE ≈ 0.01 bar. However, because the pressure data in this chemistry spans a much narrower range (~0.25 bar for SIB, compared with ~1.2 bar for LIB), the normalised error remains higher ($NRMSE_{std}$ ≈ 0.30) and the explained variance lower (R^2 ≈ 0.91) than for the LIB chemistry pressure model. This is consistent with the more scattered parity cloud and the weaker linear trend observed in **Fig. 3d**.

The LIB T_{in} estimation clearly outperforms the results for the SIB chemistry. The LIB ΔP_{in} model also achieves better relative performance, with higher R^2 and lower $NRMSE_{std}$, even though the SIB model attains a smaller absolute RMSE for ΔP_{in} owing to the reduced dynamic range of the SIB signal. These differences mirror the correlation regimes revealed by the Pearson analysis (see **Fig. 2**) and reflect how each chemistry leverages distinct aspects of the temporal model (instantaneous redundancy *vs* extended context).

Detailed error structure and cycle-resolved behaviour

To move beyond aggregate metrics, we analysed the structure of the residuals as a function of operating conditions and time. **Fig. 4** shows hexbin maps of residuals versus ground-truth values for all four tasks, while in the SI file, **Figs. S2–S6** provide complementary time-series views, histograms, range-wise error profiles, and cycle-resolved diagnostics.

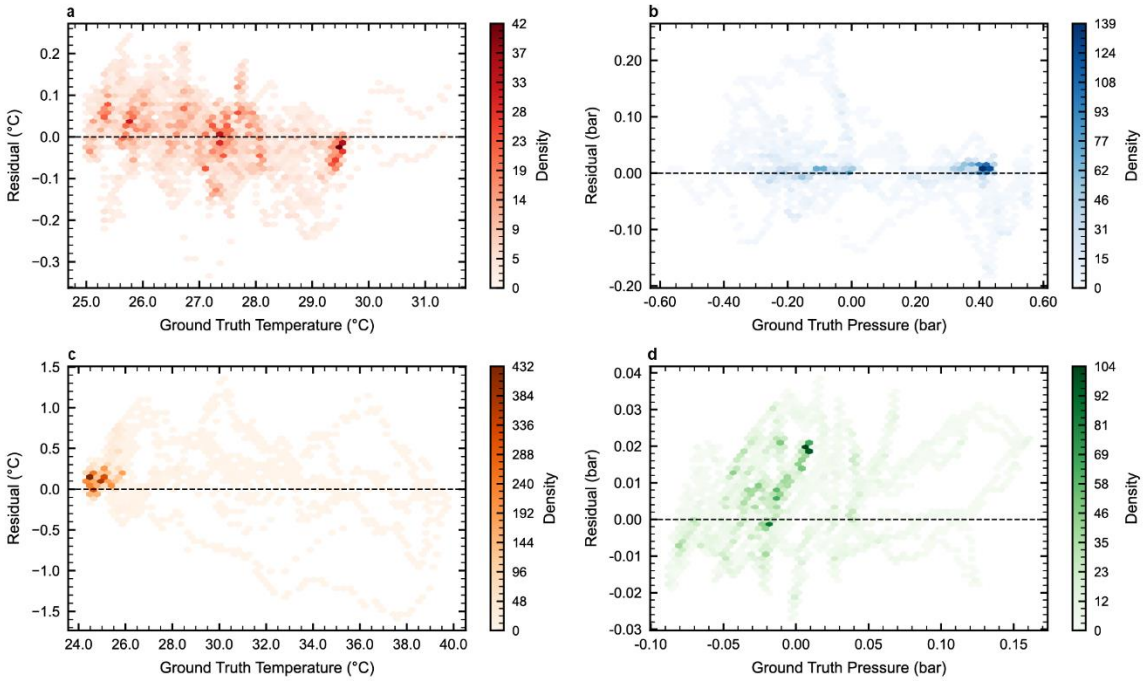


Fig. 4 Hexbin maps of residuals as functions of internal temperature and pressure. Residuals are defined as the prediction minus the ground truth. **a.** LIB internal temperature residuals versus ground truth temperature, showing a narrow band centred around zero across the full range. **b.** LIB internal pressure residuals versus ground truth pressure, with a broader band and larger spread in regions associated with stronger pressure excursions. **c.** SIB internal temperature residuals, still centred near zero but with wider dispersion and slightly larger errors at higher temperatures, when compared to the LIB data. **d.** SIB internal pressure residuals form a compact cloud with small absolute deviations over the limited pressure range explored. Colour bars indicate the density of points in each hexagonal bin. Complementary histograms, charge/discharge-resolved absolute errors, and range-wise error profiles as functions of temperature and current are provided in the SI file (**Fig. S2-S5**).

For LIB, temperature residuals (**Fig. 4a**) are narrowly concentrated around zero across the full internal temperature range, with a dense band of points tightly clustered along the horizontal axis. No pronounced systematic bias is observed, in agreement with the very small RMSE and high R^2 shown in **Fig. 3**. Pressure residuals (**Fig. 4b**) remain centred near zero but form a visibly broader band, especially in regions associated with larger pressure excursions. The spread of the residuals increases during dynamically evolving segments of the cycle, consistent with the higher $NRMSE_{std}$ for pressure relative to temperature. These patterns are corroborated by the residual histograms and charge/discharge-resolved error distributions (**Figs. S2–S3**), which show slightly heavier tails for pressure residuals and narrower spreads for temperature than for pressure, while the charge/discharge boxplots show comparable median errors and variability between charge and discharge steps.

Pressure residuals of SIB (**Fig. 4d**) form a compact cloud with small absolute deviations over the relatively narrow pressure range explored in the experiments, being also consistent with the low RMSE previous presented in **Fig. 3**. However, the residuals are more scattered when viewed in normalised terms, in line with the higher $NRMSE_{std}$ and lower R^2 of the SIB pressure model compared with its LIB counterpart. The SIB temperature residuals (**Fig. 4c**) are still centred around zero but exhibit a wider spread than for LIB, with a slight tendency towards larger errors at the upper end of the temperature range. Range-wise analyses of MAE as functions of temperature (**Fig. S4**) and current (**Fig. S5**) confirm that SIB T_{in} errors increase moderately at elevated temperatures and higher currents, whereas SIB ΔP_{in} errors show limited dependence on current across the investigated ranges.

Representative time-series for unseen charge and discharge cycles are shown in **Fig. 5**. It further illustrates that the models track both slow drifts and shorter-timescale variations in T_{in} and ΔP_{in} over entire cycles. For these same representative test cycles, cycle-resolved diagnostics based on the cumulative absolute error (**Fig. S6**) show that error growth remains bounded for both chemistries. In LIB tests, the cumulative curves evolve smoothly over charge and discharge segments, indicating stable performance over complete unseen charge–discharge trajectories (over training/validation steps). During SIB tests, cumulative error grows approximately linearly with time and shows no evidence of systematic drift, consistent with stable error accumulation over each cycle and the absence of sudden error explosions. Overall, the detailed error analysis demonstrates that the models produce physically plausible and operationally stable residual patterns. The chemistry-dependent differences observed in **Fig. 4** and **Fig. 5** are consistent with the correlation structure revealed by the Pearson analysis (**Fig. 2)** reinforcing the robustness of the proposed virtual-sensing framework across distinct cell chemistries.

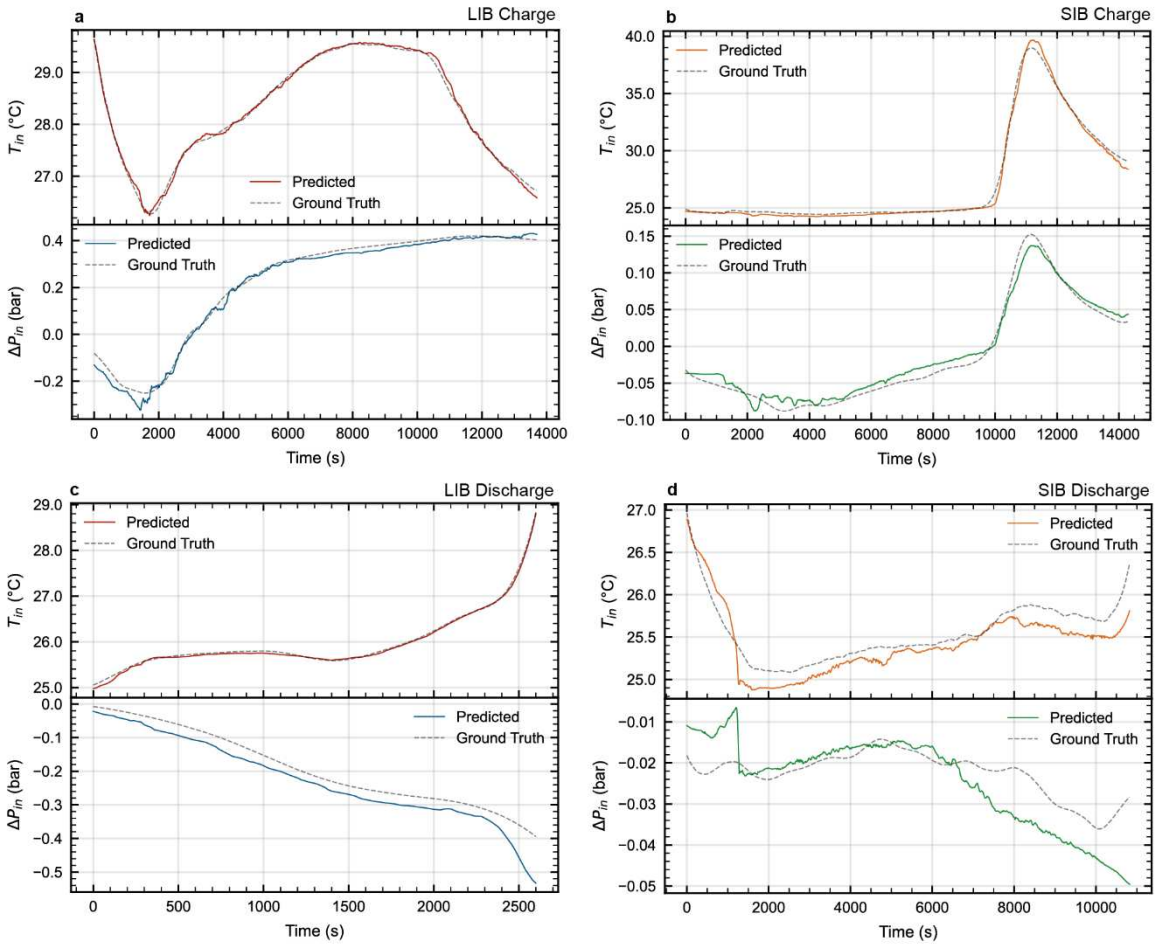


Fig. 5 Representative cycle-resolved reconstructions of internal temperature and pressure. Panels show representative charge (a,b) and discharge (c,d) cycles from the test set performed with the LIB (a,c) and SIB (b,d) batteries. In each panel, the upper plot displays the T_{in} and the lower plot the ΔP_{in}, with ground-truth measurements from the embedded hybrid OFS (dashed curves) and predictions from the chemistry-specific TCN models driven only by external features (solid curves). The close agreement over entire unseen cycles, including both slow drifts and shorter-timescale variations, illustrates the ability of the virtual sensors to track internal thermo-mechanical parameters under the tested operating conditions for both chemistries.

Model interpretability and feature reliance

To assess whether the models rely on physically meaningful information and to evaluate the robustness of their learned representations, we computed the permutation importance of all external variables for both target quantities. This analysis quantifies the degradation in predictive performance when each input feature is randomly permuted, thereby revealing the effective dependence of the trained temporal models on individual measurements. The resulting importance profiles for internal temperature and pressure, in both chemistries, are summarised in **Fig. 6**.

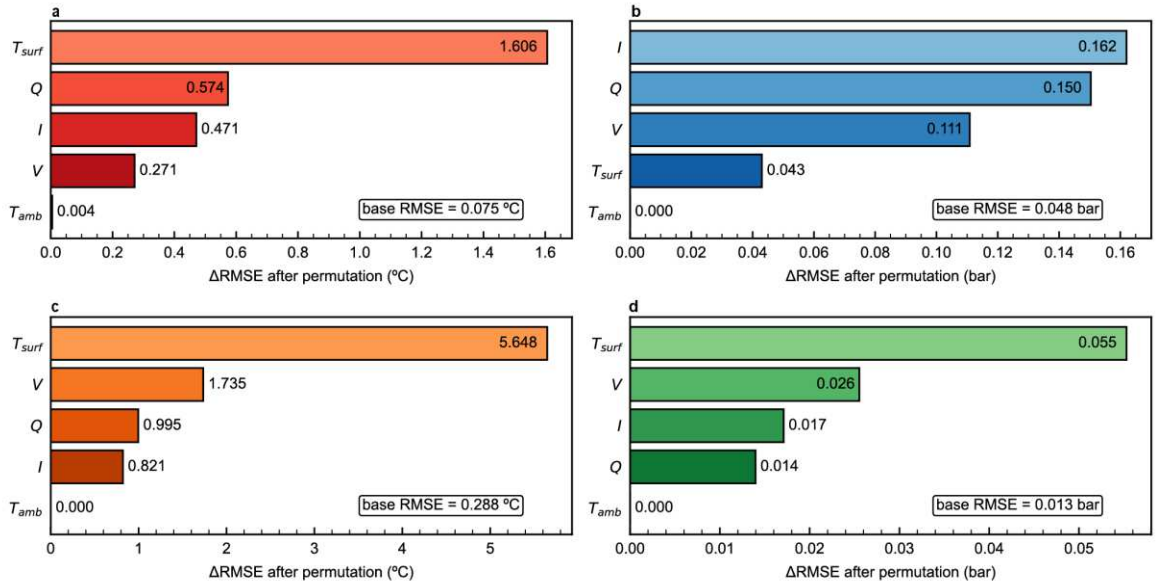


Fig. 6 Permutation importance of external features for reconstructing internal temperature and pressure. The bars report the increase in test-set RMSE ($\Delta RMSE$) obtained when each input feature is randomly permuted, for **a.** LIB internal temperature, **b.** LIB internal pressure, **c.** SIB internal temperature and **d.** SIB internal pressure. Features include surface temperature T_{surf}, ambient temperature T_{amb}, voltage V, current I, and cumulative charge Q. For both chemistries, T_{surf} dominates internal-temperature estimation, while pressure reconstruction relies on combinations of electrical and thermal variables, with voltage, charge, and (for LIB) current playing key roles. T_{amb} consistently shows negligible importance, indicating limited direct information about internal parameters under the tested conditions.

For LIB, T_{in} estimation is clearly dominated by the T_{surf} measurement (**Fig. 6a**). Permuting T_{surf} produces by far the largest increase in test-set $\Delta RMSE$, confirming that the model exploits the strong direct coupling between surface and internal temperature identified in **Fig. 2**. Electrical variables (V, I, Q) still contribute noticeably, reflecting their role in capturing electrochemical heat generation during dynamic segments of the cycle, but their permutation leads to more modest error increases. On the other hand, T_{amb} has a negligible impact, consistent with the strong thermal coupling between the cell surface and its interior, which reduces the incremental value of the environmental channel once T_{surf} is available. In contrast, LIB ΔP_{in} (**Fig. 6b**) depends on a broader combination of variables. Permuting V, Q, and I yields clear increases in error, confirming that pressure reconstruction is driven primarily by electrical load indicators and charge-storage history. T_{surf} shows a smaller but non-zero importance, suggesting a secondary thermo-mechanical contribution to pressure dynamics, while T_{amb} again remains largely irrelevant.

The SIB displays a related but distinct pattern. For internal temperature (**Fig. 6c**), T_{surf} remains the most influential variable, as in the LIB case, but the electrical features, particularly Q and V, show higher relative importance than would be expected from their

instantaneous correlations alone (**Fig. 2**). This behaviour is consistent with the longer input window (temporal context) of its model and indicates that it exploits temporally integrated electro-thermal signatures to infer T_{in} estimations, rather than relying almost exclusively on the instantaneous surface measurement. The importance patterns remain physically coherent but shift in a chemistry-dependent way. T_{in} is still most sensitive to T_{surf} (**Fig. 6c**), yet Q and V exhibit higher relative importance than in LIB, aligning with the idea that SIB thermal behaviour is encoded more diffusely and benefits from temporally integrated electro-thermal signs (consistent with the longer context selected during optimisation). Also, from SIB internal pressure results (**Fig. 6d**), V and T_{surf} become the most critical drivers, Q plays an intermediate role, and I has only a minor impact; consistent with a smoother, lower-amplitude mechanical response in which ΔP reflects a combined electro-thermal state rather than sharp current excursions. T_{amb} again contributes negligibly.

Across both chemistries and both targets, the permutation-importance profiles demonstrate that the model's privilege physically coherent channels: thermal variables for temperature reconstruction and combinations of electrical and thermal indicators for pressure.

Discussion

We demonstrate that internal temperature and pressure in both LIB and SIB can be accurately reconstructed from non-invasive measurements by combining embedded physical OFS with chemistry-adapted temporal deep-learning models. Here, generalisation is assessed at the cycle level, i.e., performance on held-out charge–discharge cycles from the same instrumented battery for each chemistry. Internal hybrid OFS provides direct measurements of thermo-mechanical states, enabling supervised training of virtual sensors that subsequently operate using only T_{surf}, T_{amb}, V, I, and Q. This strategy bridges the gap between invasive instrumentation and practical deployment, offering a route to internal-state monitoring that is compatible with standard battery packs and BMS in the final applications.

The results achieved in this work demonstrate impactful scientific implications. First, it shows that embedded physical OFS can be used as calibration tools during development rather than permanent instrumentation in the field, enabling the training of virtual sensors that exploit only non-invasive measurements. Second, it demonstrates that a single modelling framework can be applied across chemistries, provided that the architecture and temporal context (window length) are adapted to the correlation and dynamic characteristics of each system. Finally, the combination of temporal deep learning and physics-consistent interpretability offers a promising pathway for integrating internal-state

estimation into future BMS, potentially enhancing safety margins, enabling more aggressive operation, and informing degradation-aware control strategies.

As an outlook for future work, the present study focuses on single LIB and SIB under controlled laboratory conditions; extending the framework to larger battery packs, additional chemistries, and ageing trajectories will be essential to assess generalisability. Despite its strong performance, the proposed approach is inherently data-driven and may be sensitive to operational regimes not represented in the training set; learned temporal representations may therefore degrade under substantial domain shifts. Incorporating richer operating profiles, such as drive cycles and fast charging, could further stress-test the models and provide insight into their extrapolation capabilities. From a modelling standpoint, exploring architectures that explicitly encode physical constraints or multi-scale dynamics, as well as probabilistic formulations that quantify predictive uncertainty, may further improve robustness and interpretability.

Methods

Optical Fibre Sensors Fabrication and Characterization

To monitor internal thermo-mechanical parameters during battery operation, a hybrid OFS combining FBG and FPI was tailored and produced. The design, fabrication, and calibration procedures follow our previous work [29], where the sensors were shown to provide decoupled measurements of internal temperature and pressure inside commercial cylindrical batteries. Briefly, the FBG sensors are inscribed in a photosensitive single-mode fibre near an FPI cavity previously produced on the fibre tip, forming a quasi-punctual and compact multi-parameter probe. FBG sensors were also used for surface temperature monitoring on the batteries.

All OFS fabricated were individually calibrated before integration into the batteries. The FBGs were calibrated for the temperature parameter, while the hybrid FBG–FPI sensors were characterized for both pressure and temperature response. The separation of these two quantities was achieved using the matrixial method, which decouples the thermal and pressure contributions through the interferometric response. The detailed description of the optical setup and the methodology for pressure/temperature decoupling has been reported in a previous work by our group [29], which forms the experimental physical data basis for the present study.

Battery Instrumentation and Experimental Testing Protocols

Commercial 18650-format LIB (LG Chem INR18650 MH1, 3200 mAh, nominal voltage of 3.7 V) and SIB (Hakadi, 1500 mAh, nominal voltage of 3.1 V) batteries were instrumented. Two independent experimental campaigns were conducted for both chemistries. Both batteries were instrumented with the physical sensors capable of simultaneously monitoring internal parameters during galvanostatic cycling tests. The optical fibres with the physical sensors were carefully positioned near the geometric centre of the jelly-roll, through a precision micro-aperture into the core of the cell, and sealed with an epoxy resin to preserve internal pressure integrity, as detailed in Matuck *et al*. [29].

Reference measurements on non-instrumented cells indicated that the sensor integration did not measurably affect the battery capacity and performance under the conditions used in this work. In addition, an external optical fibre with two FBG sensors was positioned in each battery: one attached to the cell surface to monitor the surface temperature (T_{surf}) and another placed nearby to measure the ambient temperature (T_{amb}). The surface FBG was positioned at approximately the same axial location as the internal hybrid sensor, so that external temperature measurements corresponded to the region where the internal sensor was located. The data from the internal physical hybrid sensor thus served as the reference for internal pressure and temperature, providing the ground-truth data used for model training.

The experiments were conducted under controlled room conditions, and the batteries were cycled between predefined voltage limits using constant-current/constant-voltage (CCCV) charge and constant-current (CC) discharge protocols at different C-rates (C/3, C/4, and C/6). Each battery underwent several complete charge–discharge cycles, 34 cycles for the LIB and 27 cycles for the SIB, which were later used to construct two independent datasets, one per battery chemistry.

Data Acquisition, Pre-processing, and Feature Construction

Optical signals were continuously acquired using an optical interrogator (si155 Luna Hyperion, 4 channels, operating at a sampling rate of 0.05 Hz, equivalent to one sample every 20 s). In parallel, the electrochemical data were acquired by galvanostat/potentiostat (SP-50e, from Biologic, France). The acquisition systems shared a common timestamp reference, enabling consistent temporal alignment required for subsequent window segmentation and model training. All optical and electrochemical signals were temporally synchronized and segmented into individual charge and discharge sequences.

For ML purposes, the dataset integrated optical and electrical data from the synchronised acquisition systems. The input features consisted of external variables accessible without cell intrusion: surface and ambient temperatures (T_{surf}, T_{amb}) measured by the external FBG sensors, as well as terminal voltage (V), current (I), and cumulative charge (Q) recorded by the potentiostat. The target variables corresponded to the internal ΔP_{in} and T_{in} obtained from the hybrid sensors. This multimodal configuration provided externally measurable, non-invasive inputs for model training, while the internal optical data served as high-fidelity ground-truth references. From a ML standpoint, this setup defines a supervised temporal regression task for virtual sensing, in which internal states are inferred from externally measurable signals.

Before model training, the optical and electrical data were pre-processed following a three-step pipeline to ensure consistency and signal integrity. First, the temperature and pressure data were denoised using a *Savitzky–Golay* filter to reduce measurement noise while preserving the overall temporal trends of the signals. The filter was applied with a polynomial order of 3 and an interpolation mode to mitigate edge distortions. The window length was adjusted according to the dynamics of each variable: 31 points for all temperature-related data and 61 points for the pressure data, which exhibited higher variability and therefore required broader smoothing. In contrast, the electrical variables were left unfiltered, since their acquisition was already smooth and free from high-frequency noise artifacts. Next, all input and target variables were standardized using Z-score normalization, implemented through the *StandardScaler* method from scikit-learn. The scaler was applied with its default configuration and fitted globally on the concatenated training dataset of each chemistry, ensuring consistent scaling across all charge and discharge cycles and preventing distributional drift between subsets. The fitted parameters were subsequently applied to the validation and test sets to ensure consistent normalization while explicitly preventing data leakage..

The standardized sequences were segmented into overlapping temporal windows using a sliding-window approach with a stride of one-time step. The window length was optimized independently for each battery chemistry through Bayesian optimization with Optuna. The resulting data tensors were three-dimensional, organized as samples, time steps, and features, providing suitable input for deep temporal models such as TCN.

Finally, the data for each chemistry was randomly divided into training, validation, and testing subsets, corresponding to 70%, 15%, and 15% of the total number of complete cycles, respectively. The splitting was performed at the cycle level to prevent window-level leakage between sets and to ensure evaluation on unseen cycles. This procedure ensured that the model's evaluation reflected true generalization capability to unseen operational sequences. Fig. 1 illustrates the complete workflow adopted in this study, encompassing data acquisition, pre-processing, and model training stages.

Temporal Convolutional Network Architecture

A TCN was implemented to model the sequential dynamics of the battery data. This architecture was selected due to its capacity to capture long-range temporal dependencies while maintaining high computational efficiency, an essential feature for real-time diagnostic applications. In contrast to recurrent models, the TCN employs one-dimensional causal and dilated convolutions, ensuring that predictions at any given time depend only on current and past information, thus preserving the physical causality inherent to battery processes.

The network architecture was designed to balance representational power and generalization. The input layer receives multivariate time-series sequences with dimensions corresponding to the number of time steps and input features defined for each chemistry. The core temporal modelling is performed by a single TCN block configured with one stack and four dilation levels (1,2,4,8), which exponentially expand the effective temporal receptive field, allowing the model to capture hierarchical temporal dependencies ranging from short-term fluctuations to long-term correlations. All key architectural hyperparameters of the TCN, such as the number of convolutional filters, kernel size, and dropout rate, were optimized through Bayesian search using the Optuna framework, and it was summarized in the SI file (Table S1).

Following the temporal convolutional stage, a *LayerNormalization* operation was applied to stabilize internal activations and improve convergence. The normalized output was then passed to a fully connected dense layer with *ReLU* activation, providing a compact representation of the extracted temporal features. The final output layer consisted of two linear neurons, corresponding to the predicted *Tin* and internal ΔP_{in}.

Bayesian Hyperparameter Optimization

To ensure optimal predictive performance and fair comparison between battery chemistries, model hyperparameters were tuned automatically through Bayesian optimization using the Optuna framework. This method efficiently explores the hyperparameter space by sequentially updating a probabilistic surrogate model of the objective function, thereby identifying promising configurations with fewer training iterations than grid or random search.

Separate optimisation processes were performed for the LIB and SIB datasets to account for their distinct temporal characteristics and signal variabilities. Each Optuna study was run for 500 trials per chemistry; the Optuna sampler and model training were initialised with a fixed random seed (42) to ensure reproducibility. In each optimisation run, the objective was to minimise the mean squared error (MSE) computed on the validation set

after model training. The search space included architectural parameters such as the input window length (from 10 to 60, in steps of 10), number of TCN filters (from 32 to 128, in steps of 32), convolutional kernel size (from 3 to 11, in steps of 2), number of neurons in the dense layer (16, 64, step=16) and dropout rate (from 0.1 to 0.4), as well as training-related parameters including batch size (from 16 to 64, in steps of 16) and learning rate (from 1e-4 to 5e-3). All candidate models were trained using the same data pre-processing pipeline and the same cycle-level split between training, validation, and testing sets, ensuring comparability across trials.

Each candidate model was trained for a maximum of sixty epochs using the Adam optimizer and *EarlyStopping* callback, which monitored the validation loss with a patience of twelve epochs and had the *restore_best_weights* option enabled, ensuring that the model parameters from the epoch with the lowest validation loss were preserved. A learning rate reduction on a plateau (*ReduceLROnPlateau*, with a factor of 0.5 and a patience of six epochs) was also applied to improve convergence stability. The final selected configurations were then retrained on the combined training and validation sets before evaluation on the held-out test set.

The Bayesian optimization procedure ensured that the models developed for both battery chemistries achieved balanced complexity and predictive performance while avoiding manual bias in hyperparameter selection. Although the same TCN architecture was employed for both chemistries, the models were trained independently, and all hyperparameters were optimized separately through Bayesian search. This strategy maintained architectural consistency while allowing each model to adapt its configuration to the distinct temporal dynamics and signal characteristics of its respective chemistry.

Training and Validation Protocol

Model training was conducted independently for the LIB and SIB datasets, following an identical protocol to ensure consistency and comparability between chemistries. Each model received as input multivariate time-series sequences of externally measurable quantities (T_{surf}, T_{amb}, V, I, Q), while the T_{in} and ΔP_{in} obtained from the hybrid OFS served as supervised learning targets. The entire framework was implemented in Python using *TensorFlow* and *Keras*, enabling reproducible experimentation and efficient graphics processing unit acceleration.

All models were trained using the *Adam* optimizer with learning rates determined through Bayesian optimization. The MSE was employed as the loss function, reflecting the objective of minimizing the average deviation between predicted and measured physical quantities. Training proceeded for a maximum of sixty epochs, although convergence was

typically achieved earlier due to the use of *EarlyStopping* with the *restore_best_weights* parameter enabled, which monitored the validation loss with a patience of twelve epochs and automatically reverted to the best-performing model weights. When the validation performance plateaued for six consecutive epochs, the learning rate was automatically reduced by a factor of 0.5 through the *ReduceLROnPlateau* scheduler. This adaptive strategy helped stabilize optimization and avoid local minima while preventing overfitting.

To ensure temporal independence between training, validation, and test samples, data splitting was performed at the level of entire charge–discharge cycles. This prevented window-level leakage of temporal context and ensured evaluation on held-out, unseen cycles. The model parameters corresponding to the lowest validation loss were retained for final evaluation. After training, the best model for each chemistry was reloaded and used to generate predictions on the held-out test set, composed exclusively of unseen cycles.

Both input and output variables were standardized before training, and predictions were subsequently inverse-transformed into their physical units (degrees Celsius and bar) for evaluation. This post-processing step allowed direct physical interpretation of the results and facilitated quantitative and qualitative assessment of model performance through the comparison of predicted and measured internal states.

This protocol ensured that the model's generalization ability was evaluated under realistic conditions, reflecting its potential for deployment in embedded or online diagnostic systems. The identical training framework across chemistries further enabled direct cross-comparison of predictive behaviour and stability between the LIB and SIB models, highlighting how temporal learning and data-driven inference adapt to different electrochemical environments, reinforcing the role of ML as a tool for revealing system-specific dynamical structure from data.

Use of generative AI tools

During the preparation of this manuscript and the associated machine-learning code, the authors used ChatGPT (OpenAI) to (i) improve clarity and grammar in portions of the text and (ii) assist in diagnosing and resolving software bugs in the ML pipeline. All suggestions were reviewed, edited, and validated by the authors, who take full responsibility for the final content of the manuscript and code; the tool was not used to generate primary results, to perform data analyses, or to draw scientific discussion and conclusions.

Data availability

All data used for model training and evaluation (including the TCN implementation and Optuna optimisation) will be made available in a Zenodo repository upon publication. The repository URL will be provided in the final version of the manuscript.

Code availability

Our code is available on CodeOcean [56,57], including instructions to train all models from scratch and to perform direct inference with our provided checkpoints.

References

1. Energy Agency, I. *Global EV Outlook 2024 Moving towards Increased Affordability*. www.iea.org (2024).

2. Frith, J. T., Lacey, M. J. & Ulissi, U. A non-academic perspective on the future of lithium-based batteries. *Nat Commun* 14, 420 (2023).

3. Ngoy, K. R. *et al.* Lithium-ion batteries and the future of sustainable energy: A comprehensive review. *Renewable and Sustainable Energy Reviews* 223, 115971 (2025).

4. Nykvist, B. & Nilsson, M. Rapidly falling costs of battery packs for electric vehicles. *Nat Clim Chang* 5, 329–332 (2015).

5. Dunn, B., Kamath, H. & Tarascon, J.-M. Electrical Energy Storage for the Grid: A Battery of Choices. *Science (1979)* 334, 928–935 (2011).

6. Armand, M. & Tarascon, J.-M. Building better batteries. *Nature* 451, 652–657 (2008).

7. Phogat, P., Rawat, S., Dey, S. & Wan, M. Advancements and challenges in sodium-ion batteries: A comprehensive review of materials, mechanisms, and future directions for sustainable energy storage. *J Alloys Compd* 1020, 179544 (2025).

8. Keiner, D. *et al.* Sodium-ion battery cost projections and their impact on the global energy system transition until 2050. *J Energy Storage* 146, 119861 (2026).

9. Mariyappan, S., Desai, P., Morcrette, M. & Tarascon, J.-M. From lab to market with sustainable sodium-ion batteries. *Nat Sustain* https://doi.org/10.1038/s41893-025-01701-x (2025) doi:10.1038/s41893-025-01701-x.

10. Jiang, T. *et al.* Battery technologies for grid-scale energy storage. *Nature Reviews Clean Technology* 1, 474–492 (2025).

11. Wang, Y. *et al.* The safety aspect of sodium ion batteries for practical applications. *Journal of Energy Chemistry* 95, 407–427 (2024).

12. Chen, Y. *et al.* A review of lithium-ion battery safety concerns: The issues, strategies, and testing standards. *Journal of Energy Chemistry* 59, 83–99 (2021).

13. Yu, X., Chen, R., Gan, L., Li, H. & Chen, L. Battery Safety: From Lithium-Ion to Solid-State Batteries. *Engineering* 21, 9–14 (2023).

14. Chen, Y. *et al.* A review of lithium-ion battery safety concerns: The issues, strategies, and testing standards. *Journal of Energy Chemistry* 59, 83–99 (2021).

15. Wang, Y. *et al.* The safety aspect of sodium ion batteries for practical applications. *Journal of Energy Chemistry* 95, 407–427 (2024).

16. Lim, W.-G. *et al.* Safety of Sodium-Ion Batteries: Evaluation and Perspective from Component Materials to Cells, Modules, and Packs. *Adv Energy Mater* n/a, e05016.

17. Suganya, R., Joseph, L. M. I. L. & Kollem, S. Understanding lithium-ion battery management systems in electric vehicles: Environmental and health impacts, comparative study, and future trends: A review. *Results in Engineering* 24, 103047 (2024).

18. Gabbar, H. A., Othman, A. M. & Abdussami, M. R. Review of Battery Management Systems (BMS) Development and Industrial Standards. *Technologies (Basel)* 9, (2021).

19. Wang, C. *et al.* A review of battery SOC estimation based on equivalent circuit models. *J Energy Storage* 110, 115346 (2025).

20. Chen, S. *et al.* Advances in internal temperature measurement and estimation for lithium-ion batteries. *J Energy Storage* 140, 118950 (2025).

21. Xiang, D. *et al.* Online Monitoring of Lithium-Ion Battery Internal Temperature Using PWM Switching Oscillations. *IEEE Trans Power Electron* 38, 1166–1177 (2023).

22. Chen, H. *et al.* Experimental and numerical study of internal pressure of lithium-ion batteries under overheating. *J Energy Storage* 116, 116066 (2025).

23. García, A., Monsalve-Serrano, J., Marco Gimeno, J. & Hernández Egea, J. M. Experimental measurement and modeling of the internal pressure in cylindrical lithium-ion battery cells under abuse conditions. *J Energy Storage* 103, 114288 (2024).

24. CHANG, H., LIU, G. & GUO, L. Embedded internal temperature measurement of single Lithium-ion power batteries in battery packs under different operating conditions based on flexible sensing technology. *J Energy Storage* 125, 116903 (2025).

25. Jones, C. M., Sudarshan, M., García, R. E. & Tomar, V. Direct measurement of internal temperatures of commercially-available 18650 lithium-ion batteries. *Sci Rep* 13, 14421 (2023).

26. Pan, Y., Xu, K., Chen, Z. & Wang, K. Advanced Techniques for Internal Temperature Monitoring in Lithium-Ion Batteries: A Review of Recent Developments. *Coatings* 15, (2025).

27. Rodriguez-Ramirez, D. A. *et al.* Review of Optical Fiber Sensors: Principles, Classifications and Applications in Emerging Technologies. *Photonics* 13, (2026).

28. Han, G. *et al.* A review on various optical fibre sensing methods for batteries. *Renewable and Sustainable Energy Reviews* 150, 111514 (2021).

29. Matuck, L. *et al.* Towards smart and secure batteries: Linking pressure and temperature profiles with electrochemical behavior through hybrid optical fiber sensors. *Chemical Engineering Journal* 500, 156806 (2024).

30. Ee, Y.-J. *et al.* Lithium-Ion Battery State of Charge (SoC) Estimation with Non-Electrical parameter using Uniform Fiber Bragg Grating (FBG). *J Energy Storage* 40, 102704 (2021).

31. Novais, S. *et al.* Internal and External Temperature Monitoring of a Li-Ion Battery with Fiber Bragg Grating Sensors. *Sensors* 16, (2016).

32. Liu, Q., Yang, D., Xing, M., Yan, C. & Liu, B. Research on operating mechanism and state of battery based on fiber Fabry-Pérot cavity. *Sens Actuators A Phys* 382, 116175 (2025).

33. Liu, Q. *et al.* Simultaneous measurement of temperature and refractive index based on fiber optic Fabry–Pérot cavity in batteries. *Journal of Optics* 26, 125602 (2024).

34. Nascimento, M. *et al.* Internal strain and temperature discrimination with optical fiber hybrid sensors in Li-ion batteries. *J Power Sources* 410–411, 1–9 (2019).

35. Matuck, L., Ferreira, M. S. & Nascimento, M. Revealing a Correlation between Physical Parameters and Differential Voltage Analysis of a Commercial Li-Ion Battery Based on Fiber Optic Sensors. *Batteries* 10, (2024).

36. Wang, Y. Application-oriented design of machine learning paradigms for battery science. *NPJ Comput Mater* 11, 89 (2025).

37. Valizadeh, A. & Amirhosseini, M. H. Machine Learning in Lithium-Ion Battery: Applications, Challenges, and Future Trends. *SN Comput Sci* 5, 717 (2024).

38. Thelen, A. *et al.* Probabilistic machine learning for battery health diagnostics and prognostics—review and perspectives. *npj Materials Sustainability* 2, 14 (2024).

39. Wei, Z., He, Q. & Zhao, Y. Machine learning for battery research. *J Power Sources* 549, 232125 (2022).

40. Chemali, E., Kollmeyer, P. J., Preindl, M., Ahmed, R. & Emadi, A. Long Short-Term Memory Networks for Accurate State-of-Charge Estimation of Li-ion Batteries. *IEEE Transactions on Industrial Electronics* 65, 6730–6739 (2018).

41. Chemali, E., Kollmeyer, P. J., Preindl, M. & Emadi, A. State-of-charge estimation of Li-ion batteries using deep neural networks: A machine learning approach. *J Power Sources* 400, 242–255 (2018).

42. Ofoegbu, E. O. State of charge (SOC) estimation in electric vehicle (EV) battery management systems using ensemble methods and neural networks. *J Energy Storage* 114, 115833 (2025).

43. Álvarez Antón, J. C. *et al.* Battery state-of-charge estimator using the SVM technique. *Appl Math Model* 37, 6244–6253 (2013).

44. Rae, M. *et al.* Comprehensive machine learning approaches for modelling the state of charge of lithium-ion batteries. *J Power Sources* 646, 236929 (2025).

45. Rente, B. *et al.* Lithium-Ion Battery State-of-Charge Estimator Based on FBG-Based Strain Sensor and Employing Machine Learning. *IEEE Sens J* 21, 1453–1460 (2021).

46. Li, Y. *et al.* A hybrid machine learning framework for joint SOC and SOH estimation of lithium-ion batteries assisted with fiber sensor measurements. *Appl Energy* 325, 119787 (2022).

47. Lin, C., Xu, J., Hou, J., Liang, Y. & Mei, X. Ensemble Method With Heterogeneous Models for Battery State-of-Health Estimation. *IEEE Trans Industr Inform* 19, 10160–10169 (2023).

48. Lin, C. *et al.* Multi-model ensemble learning for battery state-of-health estimation: Recent advances and perspectives. *Journal of Energy Chemistry* 100, 739–759 (2025).

49. Kaur, K., Garg, A., Cui, X., Singh, S. & Panigrahi, B. K. Deep learning networks for capacity estimation for monitoring SOH of Li-ion batteries for electric vehicles. *Int J Energy Res* 45, 3113–3128 (2021).

50. Berecibar, M. *et al.* Critical review of state of health estimation methods of Li-ion batteries for real applications. *Renewable and Sustainable Energy Reviews* 56, 572–587 (2016).

51. Liu, L., Xu, G., Wang, Y., Wang, L. & Liu, J. Battery temperature estimation at wide C-rates using the LSTM model based on polarization characteristics. *J Energy Storage* 101, 113941 (2024).

52. Gu, X., Lei, W., Xi, J. & Song, M. Structural optimization and battery temperature prediction of battery thermal management system based on machine learning. *Case Studies in Thermal Engineering* 62, 105207 (2024).

53. Bamati, S., Chaoui, H. & Gualous, H. Enhancing Battery Thermal Management With Virtual Temperature Sensor Using Hybrid CNN-LSTM. *IEEE Transactions on Transportation Electrification* 10, 10272–10287 (2024).

54. Cho, G., Zhu, D., Campbell, J. J. & Wang, M. An LSTM-PINN Hybrid Method to Estimate Lithium-Ion Battery Pack Temperature. *IEEE Access* 10, 100594–100604 (2022).

55. Al Miaari, A. & Ali, H. M. Batteries temperature prediction and thermal management using machine learning: An overview. *Energy Reports* 10, 2277–2305 (2023).

56. Matuck L. ´Code for ‘Lithium-ion Battery Internal Parameters Prediction with Machine-Learning’. Code Ocean https://doi.org/10.24433/CO.3092906.v1 (2026). Capsule ID: 52e8723f-4066-44d9-8d60-155bd0c677ea.

57. Matuck L. ´Code for ‘Sodium-ion Battery Internal Parameters Prediction with Machine-Learning’. Code Ocean https://doi.org/10.24433/CO.9452962.v1 (2026). Capsule ID: 16d7a507-a53f-45f9-8db4-45820ad75c66.

Acknowledgements

The authors gratefully acknowledge the financial support within the scope of the project i3N, UIDB/50025/2020, UIDP/50025/2020, and LA/P/0037/2020, all financed by national funds through the Fundação para a Ciência e Tecnologia and the Ministério da Educação e Ciência of Portugal. The authors LM, MSF, and MN are also grateful for the grant 2023.01848.BD, CEECINST/00013/2021/CP2779/CT0014, and 2022.07976.CEECIND/CP1720/CT0049, respectively.

Author contributions

L.M. conceived the study, developed the machine-learning pipeline, performed the data processing and analysis, and wrote the manuscript. J.P. contributed to the machine-learning methodology and guided model development. J.F.F.M. guided model development, reviewed the manuscript, and funding acquisition. M.S.F. performed the experimental tests and reviewed the manuscript. M.N. conceived the study, performed the experimental tests, reviewed the manuscript, and supervised the work. All authors discussed the results and approved the final manuscript.

Competing interests

The authors declare no competing interests.

Additional information

Supplementary information file is available.

Supplementary Files

This is a list of supplementary files associated with this preprint. Click to download.

- SIfileManuscriptNatureMachineIntelligence2026.pdf